

All-optical artificial vortex matter in quantum fluids of light

Sergey Alyatkin,^{1,*} Carles Milián,² Yaroslav V. Kartashov,³ Kirill A. Sitnik,¹ Julian D. Töpfer,¹ Helgi Sigurdsson,^{4,5} and Pavlos G. Lagoudakis^{1,5}

¹*Hybrid Photonics Laboratory, Skolkovo Institute of Science and Technology, Territory of Innovation Center Skolkovo, Bolshoy Boulevard 30, building 1, 121205 Moscow, Russia*

²*Institut Universitari de Matemàtica Pura i Aplicada, Universitat Politècnica de València, 46022 València, Spain*

³*Institute of Spectroscopy of Russian Academy of Sciences, Fizicheskaya Str., 5, Troitsk, Moscow, 108840, Russia*

⁴*Science Institute, University of Iceland, Dunhagi 3, IS-107, Reykjavik, Iceland*

⁵*Department of Physics and Astronomy, University of Southampton, Southampton SO17 1BJ, United Kingdom*

(Dated: July 6, 2022)

Artificial lattices are a powerful tool to reveal and study key interaction mechanisms between constituents of condensed matter systems, such as antiferromagnetic interactions leading to geometric frustration [1]. Frustration in magnetic materials is evidenced in their spin degree of freedom [2], whereas in many-body quantum systems, such as Bose-Einstein condensates in optical lattices [3], coupled lasers [4], and polariton condensates [5] that are described by a complex order parameter, frustration is scarcely explored in controllable settings. Here, we realize a radically new platform to study geometric frustration using a macroscopic quantum fluid of light based on exciton-polariton condensates [6]. We design pump configurations which drive condensates into an all-optical triangular vortex lattice with each cell possessing a vortex state of charge $l = \pm 1$. The orbital angular momentum (OAM) of each vortex replaces the role of spin angular momentum in frustrated matter. Our measurements and mean-field calculations reveal that individual pairs of coupled condensates spontaneously arrange their OAM antiparallel, implying a form of artificial orbital “antiferromagnetism”, with geometric frustration appearing in the triangular graph of three condensates. Furthermore, we demonstrate emergence of frustrated phases of driven-dissipative large-scale vortex matter, and open a route towards constructing ordered vortex arrays with nearly arbitrary configurations without directly phase-imprinting or stirring the polariton fluid.

Geometric frustration can be described as an inability of a system to minimize its energy through reduction of pairwise interactions between constituent elements. A prominent example are Ising spins with binary “up” or “down” projections ($s = \pm 1$), arranged into an antiferromagnetic (AFM) triangular graph [7]. Only two pairwise interactions can be minimized at any time leaving the third at a higher energy. If the spins are allowed

to rotate freely in the graph plane, i.e. XY spins, then the system is no longer frustrated (see top schematic in Fig. 1a). In contrast to artificial spin ice [2], artificial lattices in bosonic systems have recently permitted exploring classical XY spin frustration by associating the mean field phases of coupled macroscopic wavefunctions to planar pseudospins in ultracold atoms [3], coupled lasers [4] and exciton-polariton condensates [5, 8–10]. The next step would then be to engineer a programmable condensate vortex lattice with couplings dependent on the orbital degrees of freedom to study more complex spontaneous spatial ordering and frustration. Here, we achieve this goal by exploiting all-optically controlled exciton-polariton condensates.

Microcavity exciton-polariton (hereafter *polariton*) condensates [6] are driven nonequilibrium bosonic quantum fluids in the strong light-matter coupling regime, characterised by large interaction strengths and the possibility of all-optical driving of the condensate into artificial lattices using specially designed pump landscapes [11–13]. A notable feature of polariton condensates is their nonequilibrium superfluid character [14–16], and ability to form vortices that are pinned by sample disorder [17] or through optical trapping [18–20]. Multiple polariton vortices can become ordered under non-resonant excitation as shown experimentally [21–23] and theoretically [24] with predicted superfluid chiral edge modes [25]. However, large-scale programmable vortex lattices in quantum fluids that display spontaneous behaviour (i.e. vorticity formation without any phase-imprinting) remain unexplored in driven-dissipative systems.

In this article, we report on frustration in a driven-dissipative triangular lattice of polariton condensates, exhibiting a family of stable non-periodic vortex configurations. To realize this, we all-optically engineer a lattice of trapped polariton condensates that populate a vortex state at each lattice site. For this system, spin angular momentum (SAM) can be associated with polariton OAM, defined by a superposition of the traps first excited dipole modes $|P_x\rangle \pm i|P_y\rangle$, corresponding to OAM

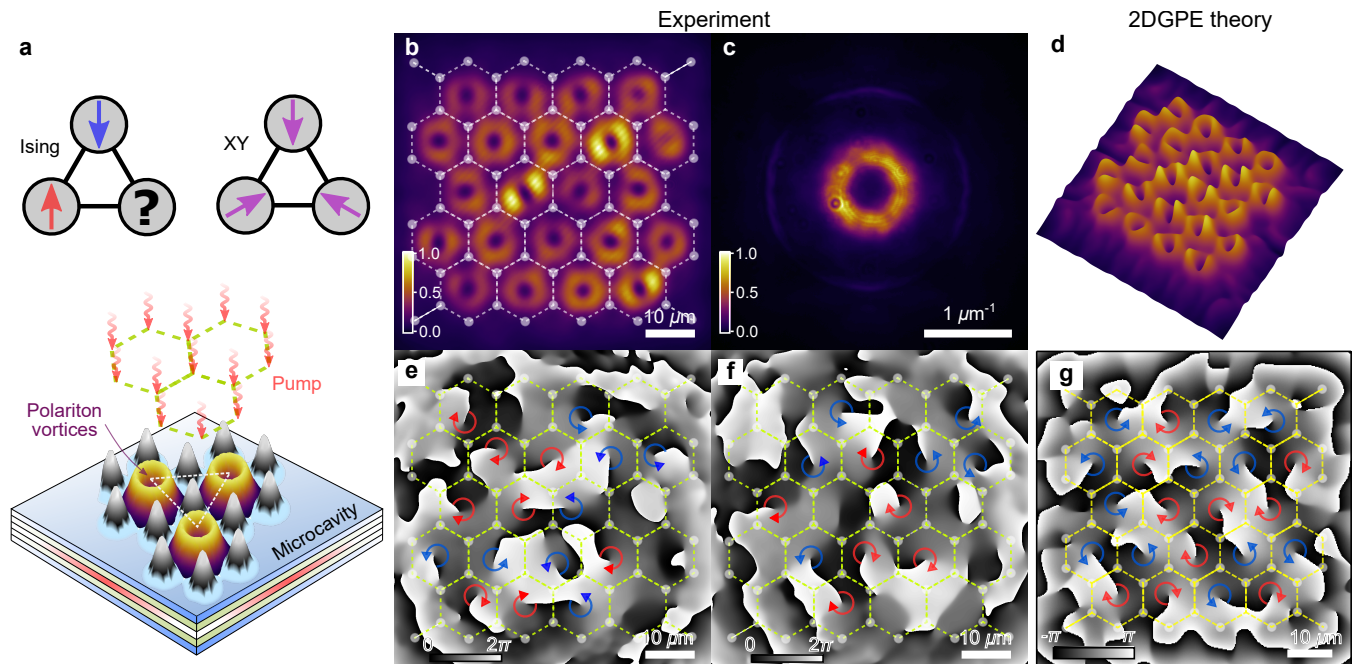


FIG. 1. **Driven triangular polariton condensate vortex lattice exhibiting frustration and multistability.** **a**, Top panels show examples of AFM frustrated triangles for the classical Ising and XY spins. The bottom panel shows schematically three polariton condensates in vortex states (yellow-violet surfaces), localised in the potential minima of the pump-induced energy landscape (black-grey surface). **b**, Experimental time-integrated real-space and **c** reciprocal-space polariton photoluminescence intensity (above condensation threshold) illustrating the formation of a large-scale vortex lattice. Overlaid honeycomb lattice in **b,e,f,g** schematically shown with dashed lines and semi-transparent circles indicates the pump positions. **e,f** Two measured single-shot realizations of the condensate phase, indicating the presence of multiple phase singularities. Blue and red arrows show schematically the phase winding direction in each cell. **d**, Single-shot realization of the condensate density and **g** phase obtained from mean field modelling.

$l = \pm 1$. Frustration in our system appears due to the incommensurate symmetries between the C_6 (sixfold rotational symmetry of the triangular lattice) and $SO(4)$ (rotation of the two-component OAM condensate) operators. Driving the system above condensation threshold results in spontaneous formation of non-periodic vortex configurations, changing from realization to realization, indicating multistability and/or stochasticity for the polaritons to condense into a definite state. We find that the large nonlinearities inherent to exciton-polariton systems are crucial for the stability of the vortices, facilitating the readout of their OAM configurations even over long excitation pulses ($\sim 10^7$ longer than the polariton lifetime).

We use a planar 2λ GaAs-based microcavity with embedded InGaAs quantum wells [26] held at ≈ 4 K in a closed-cycle helium cryostat. Using a reflective phase-only spatial light modulator (SLM), we transform an incident nonresonant single-mode continuous-wave laser beam into an ordered honeycomb array of smaller Gaussian beams focused onto the microcavity plane (see schematic bottom panel in Fig. 1a) [27]. The nonresonant pump is tuned at the first Bragg minimum of the microcavity reflectivity stop-band to avoid heating of the

sample (1.5578 eV). The x -spacing between centres of honeycomb pump cells ($D = 11.5 \mu\text{m}$) is chosen so as to obtain trapped polariton condensates in the centre of each cell [12]. Trapped condensates form due to the repulsive interactions between polaritons and the injected exciton reservoir. Polaritons drift away from the pumped region towards the potential minima of the pump-induced landscape, where they condense [28–30]. Thus, our excitation profile effectively leads to formation of a triangular lattice of potential minima as shown schematically in Fig. 1a (bottom panel).

Figure 1b shows polariton condensation into a macroscopic coherent state containing multiple vortices across the lattice for a pump power above condensation threshold (P_{thr}) unlike previous observations in square [5, 27, 31], triangular [27], and Lieb [12] optical lattices. Each cell possesses a donut shaped condensate profile corresponding to the superposition of the first excited modes of the trap. Time-integrated measurement of the reciprocal space photoluminescence (PL) in Fig. 1c also reveals a dominant donut shaped intensity profile.

The existence of a macroscopic wavefunction Ψ implies irrotational flow everywhere except at the vortex core where the phase singularity is located and parti-

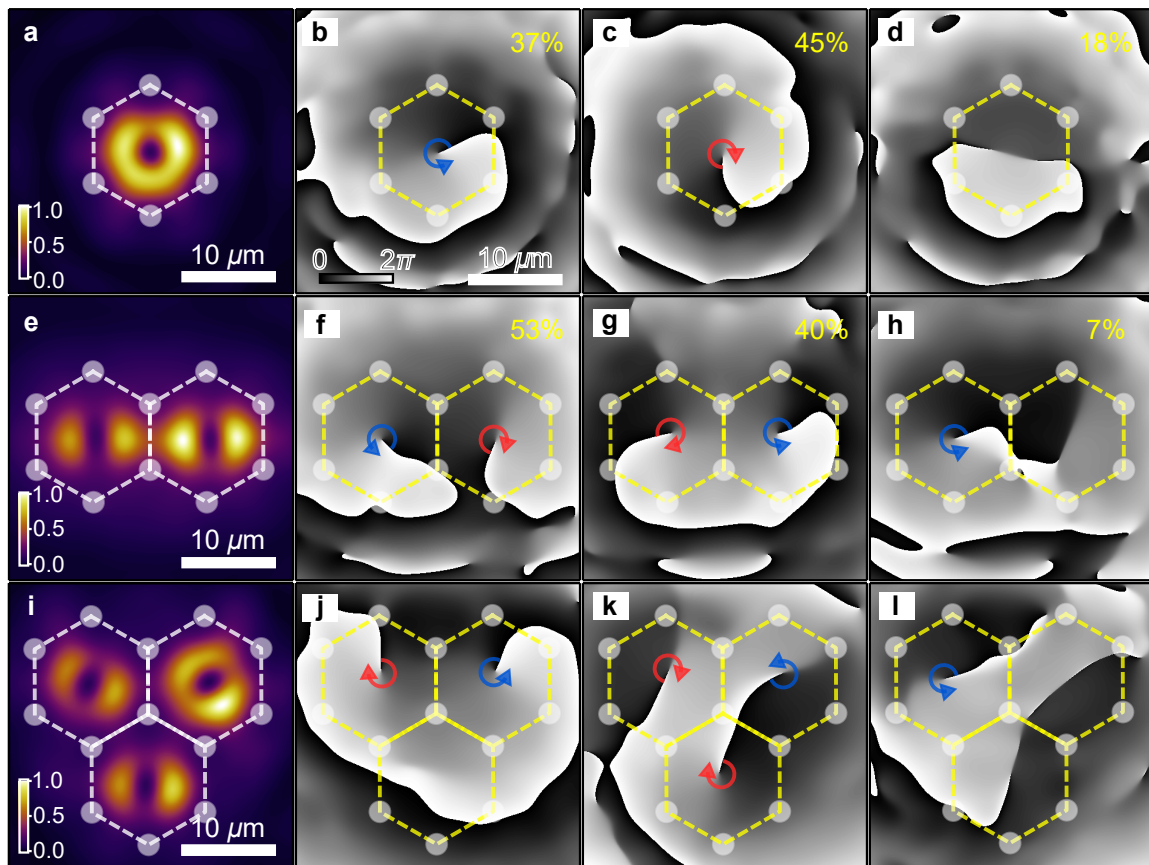


FIG. 2. **Vortices in building blocks of the lattice - single cell, two and three cells.** **a,e,i** Normalized experimentally measured time-averaged real-space polariton condensate photoluminescence for one, two and three cells, respectively. Corresponding real-space phase maps are shown in **(b-d)**, **(f-h)** and **(j-l)** panels. Dashed lines with circles schematically denote the excitation pattern. Numbers, in yellow, in **(b-d)**, **(f-h)** indicate statistical occurrence of states over one hundred single-shot realizations.

cle density vanishes. Phase winding around the core is quantized in units of $2\pi l$, where $l \in \mathbb{Z}$. In order to verify this, we apply a homodyne interferometric technique [32] to extract the phase structure of the condensate wavefunction. These phase maps examples were measured under single-shot excitation conditions, when the sample is excited by a single pulse of $50 \mu\text{s}$ duration. In Figs. 1e and 1f we show the phase maps of two individual realizations, where we observe multiple single-charge ($l = \pm 1$) phase singularities across the lattice, schematically marked by blue and red arrows. Each phase map corresponds to a single-shot realization of the polariton condensate measured over macroscopic time with respect to the cavity lifetime, indicating the topological robustness of the vortices. We note that across multiple realizations (not shown here) the phase winding configuration changes in the same spirit as shown in Figs. 1e and 1f due to the spontaneous symmetry breaking upon condensation.

The apparent random topological charge in each lattice cell (i.e. the formation of different vortex configurations

from realization-to-realization) suggests either stochasticity of charge in each cell or coexistence in this system of multiple families of vortex-carrying states revealing geometric frustration effects. To address this open question on interactions between lattice cells, we focus on a system of a few adjacent cells that could lead to macroscopic topological charge ordering and system frustration.

In order to verify the frustrated nature of our lattice, we investigate the physics of a single, a pair, and a triangle of cells (see Fig. 2). The single cell experiment allows us to confirm that the formation of vorticity is truly a spontaneous symmetry-breaking event with a random sign of vortex charge from realization-to-realization. Figure 2a shows time-integrated real-space polariton PL for a single cell pumped at $P = 1.2P_{\text{thr}}$. Measurements of the single-shot phase maps across different realizations reveal that 37% of the shots resulted in formation of a vortex ($l = +1$, Fig. 2b), and 45% in an antivortex ($l = -1$, Fig. 2c). Due to slight pump anisotropy and sample disorder, we also find that a small portion of realizations (18%) results in distributions with step-

like π phase jumps (Fig. 2d) indicating the formation of a dipolar state. The absence of a predominant sign of the observed vortex charges means that our excitation method does not break chiral symmetry and that vorticity emerges spontaneously during the polariton condensation process. In the **Methods** we show, using a simple variational generalised Gross-Pitaevskii model, that $l = \pm 1$ vortices in an ideal cylindrically symmetric optical trap (approximating the actual trap induced by six pump spots) are the only stable condensate solutions, in qualitative agreement with our observations. We emphasize that our nonresonant excitation pattern does not carry any OAM, nor does it imprint any phase onto the condensate, like in resonant excitation schemes [33].

We next focus on two coupled cells, shown in Fig. 2e, which convincingly demonstrate signatures of synchronization in experiments, as we describe below. In order to verify the antiferromagnetic nature of coupling between two cells we map the recorded OAM of each vortex state to SAM. Firstly, we point out that the recorded phase singularities in our lattice (Figs. 1e,f) are clearly distinguishable under modulated continuous-wave excitation with $50 \mu\text{s}$ pulse width - many orders of magnitude longer than any characteristic time in the system dynamics. In particular, such pulse duration is six orders of magnitude longer than the typical instability time-scales associated to the stationary modes that we report below. This already evidences coherent coupling between adjacent cells, which we now demonstrate for two cells. Figures 2f-h show three typical examples of phase maps observed in a hundred independent single-shots. Remarkably, we obtained that 93% of the condensate realizations formed vortex-antivortex (or antivortex-vortex) states with opposite topological charges in two cells. The remaining 7% correspond to vortex-dipole (or antivortex-dipole) states. Therefore, our data analysis conclusively proves that spatial coupling (tunnelling) of polaritons strongly favours AFM order for pump powers near condensation threshold. This is consistent with our mean-field model, which predicts the existence of only one lattice mode over this range of pump powers that is in the AFM state.

In Figs. 2i-l we optically construct an equilateral triangle just above condensation threshold. The system's preference for the AFM ordering as well as the expected topological charge frustration is neatly confirmed by our experimental measurements. In Fig. 2j-l we provide few examples of extracted phase maps corresponding to different configurations even though the excitation conditions (geometry and pump power) are kept the same. For example, in Fig. 2j one can see antivortex-vortex formation in two top cells and a practically smooth phase inside the bottom cell. For a different realization shown in Fig. 2k, vortices are present in all cells. Figure 2l reveals a combination of a vortex and two dipole states (characterised by an abrupt π phase slip line inside the cells). These results clearly indicate geometric frustra-

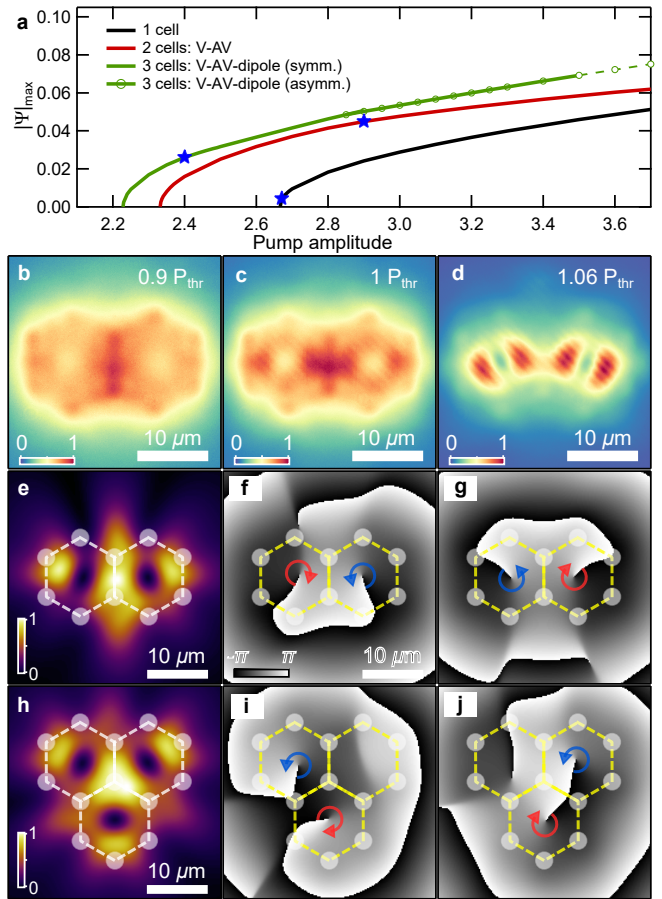


FIG. 3. Vorticity dependence on pump power. **a** Calculated dependence of the stationary amplitude of the polariton wavefunction emerging in one, two, and three cells with varying pump power. The blue stars denote the onset of vorticity with increasing power. Below these stars the polaritons dominantly localize on top of the pump spots with no apparent vorticity like in **c**. The threshold (start of solid curves) lowers when more pump spots are introduced. For the 3-cell triangle (green curve) an additional asymmetric frustrated state appears (green circles) at higher powers. **b-d** Measured real-space polariton PL for two pump cells and increasing power. **b** Below and **c** at threshold the polariton PL is mostly coming from the ridge of the pump-induced traps with no clear vortex formation. **d** At higher power the condensate collapses inside the traps forming a vortex-antivortex state. **e-j** Example solutions from 2DGPE simulation of the condensate density and phase for a pair and triangle of cells showing agreement with Fig. 2.

tion appearing in the 3-cell structure, and as it is also visible in the large-scale vortex lattice discussed in Fig. 1.

Our observations are confirmed by numerical mean-field simulations, based on the generalised two-dimensional Gross-Pitaevskii equation (2DGPE) for a macroscopic polariton wavefunction, $\Psi(\mathbf{r}, t)$, coupled to the rate equation for the exciton reservoir, $n_X(\mathbf{r}, t)$ (see **Methods**). Figures 1d and 1g show a representative example of the simulated condensate density and phase

distributions emerging from random initial conditions, clearly illustrating the formation of a vortex lattice. Excitation from random noise typically yields dynamical, breathing, structures that nevertheless are characterised by persistence of vortices, once they form in the cells. In agreement with the experiment, the arrangement of vortices changes from simulation to simulation, illustrating the highly multi-modal nature of the lattice.

In order to obtain families of possible solutions (modes) corresponding to one-, two- and three-cells pump configurations, we apply the Newton method and perform linear stability analysis. Families of stationary states evolving in time as $\Psi(\mathbf{r}, t) = w(\mathbf{r})e^{-i\varepsilon t}$ with $\partial_t n_X = 0$ (here ε is the energy detuning), which emerge as stable attractors at threshold are presented in Fig. 3a. In this graph we show the dependence of the scaled peak amplitude of the wavefunction $(g_c m_{\text{eff}} r_0^2 / \hbar^2)^{1/2} |\Psi|$ on pump power P_0 . Here, $r_0 = 1 \mu\text{m}$ is the characteristic spatial scale, m_{eff} is the polariton mass, and g_c is the polariton-polariton interaction strength. One can see that the threshold pump power decreases with increasing number of cells in the pump profile [34]. For a single honeycomb pump cell, stable vortices emerge almost at condensation threshold (blue star on black curve), in good agreement with our experiments.

Our simulations also correctly predict that for the two-cell configuration the stable branch emerging from threshold (red curve in Fig. 3a) corresponds to the branch where vortex-antivortex (AFM) states are found. Interestingly, the AFM configuration appears only above a certain critical pump amplitude (marked with a blue star on the red curve), whilst below this power, vorticity is absent and field distribution exhibits dipole structure. This critical pump power represents a vorticity threshold, clearly observed in our experiments on two cells, shown in Fig. 3b-d. Simulated time-averaged real-space intensity for such states, excited from weak noise is shown in Fig. 3e along with instantaneous phase maps for two different initial conditions in Fig. 3f,g, revealing the formation of either antivortex-vortex or vortex-antivortex pairs, similar to observations in Fig. 2e-h. We note that the existence of vorticity thresholds and corresponding values of these bifurcation points for the single and double cell systems is analytically predicted by a variational approach applied to Gross-Pitaevskii model (around the threshold) in the $l = \pm 1$ subspace (see Methods).

When we add a third pump cell, the first stationary family emanating from threshold (green curve in Fig. 3a) is associated with a vortex-antivortex-dipole configuration, which we show in Fig. 3h-i. These results are in very good agreement with observations in Fig. 2i-j. Similarly to the case of two cells, there is a vorticity threshold power, marked with a blue star on the green solid curve, below which the condensate resembles a triple dipole state. When pumped stronger than this value, the system occupies a symmetric stable vortex-antivortex-dipole

state that gradually transforms into an asymmetric solution of the same type (solid green curve with dots). Further increase of pump power results in unstable behaviour (denoted with green dashed curve in Fig. 3a) and the emergence of different stationary states $w(\mathbf{r})$, such as the antivortex-vortex-antivortex in Fig. 2k.

We note that self-arranging vortices are well-known in rotating superfluids [35], atomic BECs [36], and in nonlinear optical systems [37–40]. However, from the above discussion, it is evident that our all-optical lattice supports large scale polaritonic modes (or super-modes), which arise due to the inter-cell interactions in our nonlinear system, rather than to a collection of uncoupled individual single-site states. As such, system states are prone to develop strong instabilities that could demolish their robustness and, hence, their observation. For this reason, the observation of a large number of coupled vortices constitutes in itself a remarkable finding, that could not be anticipated *a priori*. With 22 cells (Fig. 1b) a large number of stationary states coexist for pump powers just above the condensation threshold and the system exhibits a large degree of multi-stability. As a consequence, the different experimental realizations with 22 cells reveal the formation of a wide diversity of states where individual vortex locations appear stochastically from one realization to the next.

In conclusion, we demonstrate evidence of an all-optically imprinted lattice of interacting vortices in nonresonantly driven-dissipative quantum fluids of light. Whereas in a single cell, we observe an intrinsically stochastic behaviour of an optically trapped polariton condensate, in the presence of the second neighbouring cell we reveal synchronization into a vortex-antivortex state, resembling the OAM analogue of AFM coupling. Our findings address the main challenge of realizing the node-to-node coupling in spatially confined quantum fluids of light possessing OAM. Our observations open a new avenue towards control over macroscopic ordered coherent states carrying OAM in arbitrary desired arrays. By tuning the interactions between ordered trapped polariton condensates, one can expect observation of various artificial magnetic phases between the nodes, emulating complex magnetic systems, and the study of other exotic coherent states in expanded structures.

Data availability

The datasets presented in this work are openly available from the University of Southampton repository.

* s.alyatkin@skoltech.ru

[1] Vedmedenko, E. *Competing interactions and pattern formation in nanoworld* (John Wiley & Sons, 2007).

- [2] Skjærvø, S. H., Marrows, C. H., Stamps, R. L. & Heyderman, L. J. Advances in artificial spin ice. *Nature Reviews Physics* **2**, 13–28 (2020). URL <https://doi.org/10.1038/s42254-019-0118-3>.
- [3] Struck, J. *et al.* Quantum simulation of frustrated classical magnetism in triangular optical lattices. *Science* **333**, 996–999 (2011). URL <https://www.science.org/doi/abs/10.1126/science.1207239>.
- [4] Nixon, M., Ronen, E., Friesem, A. A. & Davidson, N. Observing geometric frustration with thousands of coupled lasers. *Phys. Rev. Lett.* **110**, 184102 (2013). URL <https://link.aps.org/doi/10.1103/PhysRevLett.110.184102>.
- [5] Berloff, N. G. *et al.* Realizing the classical xy hamiltonian in polariton simulators. *Nature Materials* **16**, 1120–1126 (2017). URL <https://doi.org/10.1038/nmat4971>.
- [6] Carusotto, I. & Ciuti, C. Quantum fluids of light. *Rev. Mod. Phys.* **85**, 299–366 (2013). URL <https://link.aps.org/doi/10.1103/RevModPhys.85.299>.
- [7] Wannier, G. H. Antiferromagnetism. the triangular ising net. *Phys. Rev.* **79**, 357–364 (1950). URL <https://link.aps.org/doi/10.1103/PhysRev.79.357>.
- [8] Ohadi, H. *et al.* Nontrivial phase coupling in polariton multiplets. *Phys. Rev. X* **6**, 031032 (2016). URL <https://link.aps.org/doi/10.1103/PhysRevX.6.031032>.
- [9] Cookson, T. *et al.* Geometric frustration in polygons of polariton condensates creating vortices of varying topological charge. *Nature Communications* **12**, 2120 (2021). URL <https://doi.org/10.1038/s41467-021-22121-3>.
- [10] Tao, R. *et al.* Halide perovskites enable polaritonic XY spin hamiltonian at room temperature. *Nature Materials* **21**, 761–766 (2022). URL <https://doi.org/10.1038/s41563-022-01276-4>.
- [11] Pickup, L., Sigurdsson, H., Ruostekoski, J. & Lagoudakis, P. G. Synthetic band-structure engineering in polariton crystals with non-hermitian topological phases. *Nature Communications* **11**, 4431 (2020). URL <https://doi.org/10.1038/s41467-020-18213-1>.
- [12] Alyatkin, S., Sigurdsson, H., Askitopoulos, A., Töpfer, J. D. & Lagoudakis, P. G. Quantum fluids of light in all-optical scatterer lattices. *Nature Communications* **12** (2021). URL <https://doi.org/10.1038/s41467-021-25845-4>.
- [13] Pieczarka, M. *et al.* Topological phase transition in an all-optical exciton-polariton lattice. *Optica* **8**, 1084–1091 (2021). URL <http://opg.optica.org/optica/abstract.cfm?URI=optica-8-8-1084>.
- [14] Amo, A. *et al.* Superfluidity of polaritons in semiconductor microcavities. *Nature Physics* **5**, 805–810 (2009). URL <https://doi.org/10.1038/nphys1364>.
- [15] Sanvitto, D. *et al.* Persistent currents and quantized vortices in a polariton superfluid. *Nature Physics* **6**, 527–533 (2010). URL <https://doi.org/10.1038/nphys1668>.
- [16] Lerario, G. *et al.* Room-temperature superfluidity in a polariton condensate. *Nature Physics* **13**, 837–841 (2017). URL <https://doi.org/10.1038/nphys4147>.
- [17] Lagoudakis, K. G. *et al.* Quantized vortices in an exciton-polariton condensate. *Nature Physics* **4**, 706–710 (2008). URL <https://doi.org/10.1038/nphys1051>.
- [18] Dall, R. *et al.* Creation of orbital angular momentum states with chiral polaritonic lenses. *Phys. Rev. Lett.* **113**, 200404 (2014). URL <https://link.aps.org/doi/10.1103/PhysRevLett.113.200404>.
- [19] Gao, T. *et al.* Chiral modes at exceptional points in exciton-polariton quantum fluids. *Phys. Rev. Lett.* **120**, 065301 (2018). URL <https://link.aps.org/doi/10.1103/PhysRevLett.120.065301>.
- [20] Ma, X. *et al.* Realization of all-optical vortex switching in exciton-polariton condensates. *Nature Communications* **11** (2020). URL <https://doi.org/10.1038/s41467-020-14702-5>.
- [21] Tosi, G. *et al.* Geometrically locked vortex lattices in semiconductor quantum fluids. *Nature Communications* **3**, 1243 (2012). URL <https://doi.org/10.1038/ncomms2255>.
- [22] Gao, T. *et al.* Controlled ordering of topological charges in an exciton-polariton chain. *Phys. Rev. Lett.* **121**, 225302 (2018). URL <https://link.aps.org/doi/10.1103/PhysRevLett.121.225302>.
- [23] Sitnik, K. A. *et al.* Spontaneous formation of time-periodic vortex cluster in nonlinear fluids of light. *Phys. Rev. Lett.* **128**, 237402 (2022). URL <https://link.aps.org/doi/10.1103/PhysRevLett.128.237402>.
- [24] Keeling, J. & Berloff, N. G. Spontaneous rotating vortex lattices in a pumped decaying condensate. *Phys. Rev. Lett.* **100**, 250401 (2008). URL <https://link.aps.org/doi/10.1103/PhysRevLett.100.250401>.
- [25] Sigurdsson, H., Li, G. & Liew, T. C. H. Spontaneous and superfluid chiral edge states in exciton-polariton condensates. *Phys. Rev. B* **96**, 115453 (2017). URL <https://link.aps.org/doi/10.1103/PhysRevB.96.115453>.
- [26] Cilibrizzi, P. *et al.* Polariton condensation in a strain-compensated planar microcavity with ingaas quantum wells. *Applied Physics Letters* **105**, 191118 (2014). URL <https://doi.org/10.1063/1.4901814>.
- [27] Töpfer, J. D. *et al.* Engineering spatial coherence in lattices of polariton condensates. *Optica* **8**, 106–113 (2021). URL <http://www.osapublishing.org/optica/abstract.cfm?URI=optica-8-1-106>.
- [28] Askitopoulos, A. *et al.* Polariton condensation in an optically induced two-dimensional potential. *Physical Review B* **88** (2013). URL <https://doi.org/10.1103/physrevb.88.041308>.
- [29] Askitopoulos, A. *et al.* Robust platform for engineering pure-quantum-state transitions in polariton condensates. *Phys. Rev. B* **92**, 035305 (2015). URL <https://link.aps.org/doi/10.1103/PhysRevB.92.035305>.
- [30] Schneider, C. *et al.* Exciton-polariton trapping and potential landscape engineering. *Reports on Progress in Physics* **80**, 016503 (2016). URL <https://doi.org/10.1088/0034-4885/80/1/016503>.
- [31] Ohadi, H. *et al.* Synchronization crossover of polariton condensates in weakly disordered lattices. *Phys. Rev. B* **97**, 195109 (2018). URL <https://link.aps.org/doi/10.1103/PhysRevB.97.195109>.
- [32] Alyatkin, S., Töpfer, J., Askitopoulos, A., Sigurdsson, H. & Lagoudakis, P. Optical control of couplings in polariton condensate lattices. *Physical Review Letters* **124** (2020). URL <https://doi.org/10.1103/physrevlett.124.207402>.
- [33] Boulrier, T. *et al.* Injection of orbital angular momentum and storage of quantized vortices in polariton superfluids. *Phys. Rev. Lett.* **116**, 116402 (2016). URL <https://link.aps.org/doi/10.1103/PhysRevLett.116.116402>.
- [34] Cristofolini, P. *et al.* Optical superfluid phase transitions and trapping of polariton condensates. *Phys. Rev. Lett.* **110**, 186403 (2013). URL <https://link.aps.org/doi/10.1103/PhysRevLett.110.186403>.

- [35] Donnelly, R. J. *Quantized vortices in helium II*, vol. 2 (Cambridge University Press, 1991).
- [36] Fetter, A. L. Rotating trapped Bose-Einstein condensates. *Rev. Mod. Phys.* **81**, 647–691 (2009). URL <https://link.aps.org/doi/10.1103/RevModPhys.81.647>.
- [37] Brambilla, M. *et al.* Transverse laser patterns. I. phase singularity crystals. *Physical Review A* **43**, 5090–5113 (1991). URL <https://doi.org/10.1103/physreva.43.5090>.
- [38] Scheuer, J. Optical vortices crystals: Spontaneous generation in nonlinear semiconductor microcavities. *Science* **285**, 230–233 (1999). URL <https://doi.org/10.1126/science.285.5425.230>.
- [39] Desyatnikov, A. S., Kivshar, Y. S. & Torner, L. Optical vortices and vortex solitons. *Progress in Optics* **47**, 291–391 (2005). URL [https://doi.org/10.1016/S0079-6638\(05\)47006-7](https://doi.org/10.1016/S0079-6638(05)47006-7).
- [40] Piccardo, M. *et al.* Vortex laser arrays with topological charge control and self-healing of defects. *Nature Photonics* (2022). URL <https://doi.org/10.1038/s41566-022-00986-0>.
- [41] Wouters, M. & Carusotto, I. Excitations in a nonequilibrium Bose-Einstein condensate of exciton polaritons. *Phys. Rev. Lett.* **99**, 140402 (2007). URL <https://link.aps.org/doi/10.1103/PhysRevLett.99.140402>.
- [42] Cherotchenko, E. D., Sigurdsson, H., Askitopoulos, A. & Nalitov, A. V. Optically controlled polariton condensate molecules. *Phys. Rev. B* **103**, 115309 (2021). URL <https://link.aps.org/doi/10.1103/PhysRevB.103.115309>.

Acknowledgements

This work was supported by the Russian Science Foundation (RSF) grant no. 21-72-00088. The authors acknowledge the support of European Union’s Horizon 2020 program, through a FET Open research and innovation action under the grant agreement No. 899141 (PoLLoC). H.S. acknowledges the Icelandic Research Fund (Rannis), grant No. 217631-051.

Author contributions

S.A., J.D.T. performed experiments, S.A., J.D.T. and K.S. analyzed the data, C.M., Y.K., H.S. performed simulations, H.S. developed the variational treatment of the Gross-Pitaevskii model and derived vortex bifurcation thresholds, P.L. and Y.K. led the project, all authors contributed to discussions and writing of the manuscript.

Competing interests

The authors declare no competing interests.

Methods

Generalised Gross-Pitaevskii model. The condensate dynamics is assumed to be described by the 2D generalised Gross-Pitaevskii equation (2DGPE) for the polariton wavefunction $\Psi(\mathbf{r}, t)$ coupled to a rate equation describing the exciton reservoir feeding the condensate

$n_X(\mathbf{r}, t)$ [41]:

$$i\hbar \frac{\partial \Psi}{\partial t} = \left[-\frac{\hbar^2 \nabla^2}{2m_{\text{eff}}} - i\frac{\hbar}{2}(\gamma_c - Rn_X) + g_c |\Psi|^2 + g_r (n_X + \eta P(\mathbf{r})) \right] \Psi, \quad (1)$$

$$\frac{\partial n_X}{\partial t} = -(\gamma_X + R|\Psi|^2)n_X + P(\mathbf{r}). \quad (2)$$

Our parameters are based on the sample properties and past experiments [26]. Here, $m_{\text{eff}} \approx 5.63 \times 10^{-5} m_e$ is the effective mass of the lower-branch polaritons where m_e is the free electron rest mass, $g_c = 2.4 \mu\text{eV}\mu\text{m}^2$ is the polariton-polariton and $g_r = 2g_c$ is the polariton-reservoir interaction strengths typical for GaAs-based systems, $R = 0.021 \mu\text{m}^2\text{ps}^{-1}$ is fitted rate of stimulated scattering of polaritons from active reservoir, $\gamma_c \approx 0.182 \text{ ps}^{-1}$ and $\gamma_X \approx 0.050 \text{ ps}^{-1}$, are the decay rates for polariton condensate and reservoir excitons, respectively, $\eta\gamma_X \approx 0.49$ quantifies an additional blueshift coming from a background of dark reservoir excitons. The function $P(\mathbf{r}) = (P_0\gamma_X\gamma_c/R) \sum_n Q(\mathbf{r}-\mathbf{r}_n)$ describes spatial pump profile consisting of identical Gaussian spots $Q(\mathbf{r}) = e^{-r^2/d^2}$ of width d (corresponding to 2.5 μm -wide pump spots used in the experiment) placed in the points with coordinates \mathbf{r}_n defining particular pump configuration (one or several honeycomb cells or large-scale honeycomb lattice with period D). Dimensionless pump amplitude P_0 is defined here in units of $\gamma_X\gamma_c/R$ corresponding to condensation threshold for spatially uniform pump.

The system (1)-(2) was solved using a variant of split-step fast Fourier transform method combined with fourth-order Runge-Kutta method to account for interaction between the condensate and the reservoir. To uncover all existing stationary states in the system and possible types of evolution, including essentially dynamical regimes, when excitation of stationary states does not occur, the modeling was initiated using different realizations of small-scale noise for initial Ψ, n_X distributions. To account for considerable ballistic expansion of polaritons from the pumped regions leading to nonzero polariton density even far from them, we used in modeling sufficiently large spatial domain $300 \times 300 \mu\text{m}^2$ greatly exceeding the pumped area. Stationary states of the system (1)-(2) corresponding to $\partial_t n_X = 0$ were found in the form $\Psi(\mathbf{r}, t) = w(\mathbf{r})e^{-i\varepsilon t}$, where $w(\mathbf{r})$ is a complex function describing stationary polariton distribution in the cavity plane, ε is the energy detuning, using Newton iteration method. Due to the dissipative nature of our system, the energy detuning ε of stationary states, some of which appear as stable attractors, is also determined by the pump amplitude P_0 . Stability of such stationary states, whose families are presented in Fig. 3 for different pump configurations, were tested by modeling their evolution in the system (1)-(2) and by performing linear

stability analysis on them.

Single condensate vortex bifurcation. Here, we will write a variational form of the generalised Gross-Pitaevskii model describing only the dynamics of the first excited degenerate pair of $l = \pm 1$ OAM modes in the condensate. We will then proceed to prove, for an ideal cylindrically symmetric trap, that the only (and equally) stable condensate solutions correspond to these OAM modes.

We will assume for simplicity, that the cw driven excitonic reservoir follows the condensate adiabatically so that $\partial_t n_X \simeq 0$ which implies, $n_X = \frac{P(\mathbf{r})}{\gamma_X + R|\Psi|^2} \approx \frac{P(\mathbf{r})}{\gamma_X} \left(1 - \frac{R|\Psi|^2}{\gamma_X}\right)$. In the last step we have Taylor expanded the reservoir solution around small $R|\Psi|^2/\gamma_X$ which is valid at pump powers not too far from threshold. This allows us to write a simpler 2DGPE,

$$i\hbar \frac{\partial \Psi}{\partial t} = \left[-\frac{\hbar^2 \nabla^2}{2m_{\text{eff}}} + g_c |\Psi|^2 - \frac{i\hbar\gamma_c}{2} + g_r \eta P(\mathbf{r}) + \left(g_r + i\frac{\hbar R}{2} \right) \frac{P(\mathbf{r})}{\gamma_X} \left(1 - \frac{R|\Psi|^2}{\gamma_X} \right) \right] \Psi. \quad (3)$$

We are interested in a condensate that occupies the degenerate pair of clockwise and anticlockwise OAM states. Assuming an ideal cylindrically symmetric trap $P(\mathbf{r}) = P(r)$ we can write our truncated basis as,

$$\Psi(\mathbf{r}) = \xi(r) (\psi_+ e^{i\theta} + \psi_- e^{-i\theta}). \quad (4)$$

Here, $\xi(r)$ is the radial steady state ($\partial_t |\Psi|^2 = 0$) part of the condensate in a single optical trap by solving the 2DGPE. Plugging in this truncated solution into (3) and integrating over the space, exploiting the orthogonality of the states, we arrive at two coupled equations of motion describing the vortex phase and occupation,

$$i \frac{d\psi_{\pm}}{dt} = \left[i\tilde{p} + (\tilde{g}_c - i\tilde{R})(|\psi_{\pm}|^2 + 2|\psi_{\mp}|^2) \right] \psi_{\pm}, \quad (5)$$

up to an overall energy shift. Note the factor 2 in the counter-rotating nonlinearity (cross-Kerr term) which is orders of magnitude larger than the singlet interaction strength in spinor polariton condensates. The new coefficients are given by, $\tilde{p} = \frac{P_0 \gamma_c}{2} \int \xi(r)^2 Q(r) d\mathbf{r} - \frac{\gamma_c}{2}$, $\tilde{g}_c = \frac{g_c}{\hbar} \int \xi(r)^4 d\mathbf{r} - \frac{P_0 g_r \gamma_c}{\hbar \gamma_X} \int \xi(r)^4 Q(r) d\mathbf{r}$, and $\tilde{R} = \frac{P_0 R \gamma_c}{2 \gamma_X} \int \xi(r)^4 Q(r) d\mathbf{r}$. Equation (5) can be written in terms of the amplitude and phase of each mode $\psi_{\pm} = \sqrt{N_{\pm}} e^{i\phi_{\pm}}$,

$$\frac{dN_{\pm}}{dt} = 2 \left(\tilde{p} - \tilde{R}N_{\pm} - 2\tilde{R}N_{\mp} \right) N_{\pm}, \quad (6a)$$

$$\frac{d\phi_{\pm}}{dt} = \tilde{g}_c (N_{\pm} + 2N_{\mp}). \quad (6b)$$

We see that the change in the phase of the modes is trivially determined by the dynamics of their amplitudes.

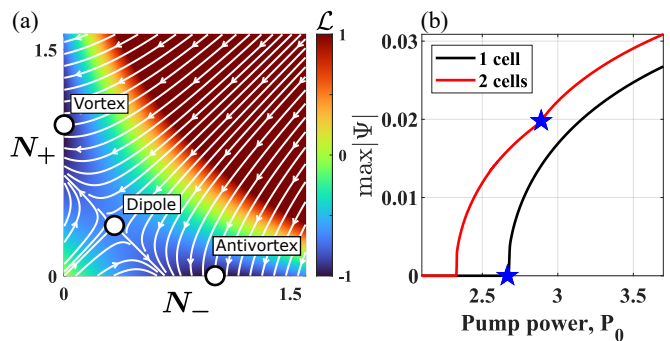


FIG. 4. **Vortex bifurcation of the single and pair of trapped condensate cells.** **a** The colorscale depicts the Lyapunov potential (7) of the system with two minima (white dots) corresponding to vortex and antivortex solutions in which all phase space trajectories converge towards, underlining the deterministic nature of the system. Here we set $\tilde{p} = R = 1$ without loss of generality. **b** Reproduced results from Fig. 3a using the variational Gross-Pitaevskii model for a single (5) and a pair of coupled condensates (9). The blue stars denote the onset of vorticity for increasing power.

We therefore only need to focus on solutions of equation (6a) which has three equilibrium points: $N_{\pm} = 0$ and $N_{\mp} = \tilde{p}/\tilde{R}$; and $N_+ = N_- = \tilde{p}/3\tilde{R}$. It is easy to show that the only (and equally) stable equilibrium points are the former through the eigenvalues λ of the Jacobian of equations (6a). This can also be visualized by plotting the system Lyapunov potential with extrema corresponding to these solutions,

$$\mathcal{L} = -2\tilde{p}(N_+ + N_-) - \tilde{R}(N_+^2 + N_-^2) - 4\tilde{R}N_+N_-. \quad (7)$$

The Lyapunov potential satisfies the condition $d\mathcal{L}/dt \leq 0$ which means that all points in phase space flow towards the two minima indicated by the white dots in Fig. 4a corresponding to the two opposite vortex solutions. The unstable saddle point extremum, corresponding to a dipole solution, is also clearly visible. Our simple model evidences that the only stable condensate solutions in a single cell are vortices which is in agreement with experiment.

These vortex solutions bifurcate from the uncondensed normal phase $N_{\pm} = 0$ at condensation threshold of the single trap written,

$$P_{0,\text{thr}}^{\text{1cell}} = P_{0,\text{vort}}^{\text{1cell}} = \left(\int \xi(r)^2 Q(r) d\mathbf{r} \right)^{-1}. \quad (8)$$

The above integral quantifies the amount of overlap between the condensate and the pumped region. If this overlap increases, then the threshold is lowered as expected.

Vortex bifurcation for two coupled condensates. The equations describing two coupled trapped condensates

read,

$$i \frac{d\psi_{n,\pm}}{dt} = \left[i\tilde{p} + (\tilde{g}_c - i\tilde{R})(|\psi_{n,\pm}|^2 + 2|\psi_{n,\mp}|^2) \right] \psi_{n,\pm} + J_a \psi_{3-n,\pm} + J_b \psi_{3-n,\mp}, \quad (9)$$

where $n = 1, 2$ denote the left and right condensate. Here, $J_{a,b} \in \mathbb{C}$ are the non-Hermitian tunneling rates between co-rotating and counter-rotating vortices (i.e. OAM conserving and non-conserving coupling strengths, respectively), $J_{a,b} = \left(\frac{g_r(1+\gamma_X\eta)}{\hbar} + i\frac{R}{2} \right) \frac{P_0\gamma_c}{R} I_{a,b}$, where

$$I_{a,b} = \int \xi(r)^* e^{\mp i\theta} Q_{\text{tot}}(\mathbf{r}) \xi(r') e^{i\theta'} d\mathbf{r}, \quad \in \mathbb{R}. \quad (10)$$

Here, $Q_{\text{tot}}(\mathbf{r})$ describes the two pumped traps and the separation between them can be written $\mathbf{r}' - \mathbf{r} = d\hat{\mathbf{x}}$. The coordinates of the two pumps are related through $r' = |\mathbf{r}'| = \sqrt{r^2 + d^2 - 2rd \cos(\theta)}$ and $\sin(\theta') = r \sin(\theta)/r'$.

Physically, $\text{Re}(J_{a,b})$ and $\text{Im}(J_{a,b})$ correspond to a Josephson (particle conserving) and dissipative (particle non-conserving), respectively, coupling between the condensates. Calculating the integral (10) numerically using the single-cell wavefunction found from 2DGPE simulations we find that $I_{a,b} < 0$ which means $\text{Im}(J_{a,b}) < 0$ and therefore the dissipative coupling favours anti-phase synchronisation between neighbouring condensates. This is

in agreement with observations in experiment Fig. 2e-h and 2DGPE simulations Fig. 3e-g. The negative value of the integral intuitively makes sense because anti-phase displaced vortices constructively interfere between the two cells. Thus anti-phase condensates overlap more strongly with the pumped region between the traps and are populated more efficiently.

The lowest threshold solution of the coupled system (9) is then written $\boldsymbol{\psi} = (\psi_{1,+}, \psi_{1,-}, \psi_{2,+}, \psi_{2,-})^T = \sqrt{N}(1, 1, -1, -1)^T e^{-i\omega t}$ with occupation $N = [\tilde{p} + |\text{Im}(J_a + J_b)|]/3\tilde{R}$ and frequency $\omega = 3N + |\text{Re}(J_a + J_b)|$. This is a antiphase dipole-dipole orientated head-to-tails (∞) \leftrightarrow (∞) with a condensation threshold of $\tilde{p}_{\text{thr}} = -|\text{Im}(J_a + J_b)|$, in agreement with previous predictions [42]. Such anisotropic low-threshold solution intuitively makes sense since polaritons flow stronger out of the trap parallel to the condensate dipole axis, thus creating optimal coupling (overlap) conditions between two spatially interacting condensates (e.g., similar to σ -bonding in chemistry). At higher pump powers these dipoles in each condensate loose stability and bifurcate each into either $l = \pm 1$ vortices. When $|I_b| > |I_a|$ the system favours AFM ordering, like reported in Fig. 2e-h. If $|I_b| < |I_a|$ the converse is true and FM ordering is dominant. This vortex bifurcation point $P_{0,\text{vort}}^{2\text{cells}}$ can be analytically derived for the AFM case $|I_b| > |I_a|$ (The FM case follows similar treatment) by locating the onset of linear instability for the dipole-dipole solution,

$$P_{0,\text{vort}}^{2\text{cells}} = \frac{1 + \frac{4g_c^2(1 + \gamma_X\eta)}{R^2} \left(2 - \frac{\gamma_X}{\gamma_c} \frac{\int \xi(r)^4 d\mathbf{r}}{\int \xi(r)^4 Q(r) d\mathbf{r}} (I_a + I_b) \right)}{I_p \left(1 + \frac{8g_c^2(1 + \gamma_X\eta)}{R^2} \right) + \left(2I_a + 3I_a \left(\frac{4g_c(1 + \gamma_X\eta)}{R} \right)^2 - I_b - 2 \frac{4g_c^2(1 + \gamma_X\eta)}{R^2} (I_a + I_b) \right)}. \quad (11)$$

Note that $I_{a,b} < 0$ which means that if the coupling anisotropy I_b/I_a is large then the critical power of the AFM vortex bifurcation reduces. This means that by tailoring the pump $P_{\text{tot}}(\mathbf{r})$ one can adjust $I_{a,b}$ to shift the position of the bifurcation point.

We obtain good results shown in Fig. 4b using $I_{a,b}$ as fitting parameters and solving the variational Gross-

Pitaevskii equation for a single cell (5) and two cells (9) as a function of increasing power. Our results are in excellent agreement with 2DGPE simulations previously shown in Fig. 3a, and thus explain the essential observations of our experiment. The blue stars indicate the onset of vorticity in the system.